Supplementary Material to the article „Thermal bottleneck in a freely suspended superconducting island on InAs nanowire“

DEVICES

Details of the molecular beam epitaxy growth of the nanowires (NWs) are given in [1]. The devices studied in the main text are distributed across three substrates: D1 on one substrate; D2, D3, D4 on another; and D5, D6 on the third. Several NWs have appeared in our previous works: D5 was labeled IIE in [1] and D2 in [2]; D3 and D4 correspond to D1 and D5 in [2], respectively. For the previously unreported devices, we provide additional images in Fig. S1a-c. For device D1, the top contact pads were fabricated by optical lithography and magnetron sputtering of aluminum (thickness 250 nm). Bright stripes crossing the NW, visible in Fig. S1a and Fig. 1b of the main text, are non-conducting residues of baked resist. These residues were removed by ultrasonic cleaning in acetone before the measurements. For all other devices (D2–D6), the top contact pads were fabricated by thermal evaporation of Cr/Au (2.5 nm/250 nm).

From the fits of the critical Joule power as a function of the magnetic field we obtain the InAs core radius $\rho_{\rm i}$ in each device. The Al shell thickness is taken as $t = 42$ nm and the superconducting coherence length as $\xi_0 = 156$ nm in all devices. The length L of the Al island (S-island) was estimated using scanning electron microscope images. Table S1 summarizes the device parameters and the extracted environmental cooling parameter $\Sigma_{\rm env}$ for the three-temperature model (3TM) presented in Figs. 2 and Figs. 3 of the main text. The electron-phonon cooling power is fixed at $\Sigma_{\rm e-ph} = 5.2\ {\rm nW}\,\mu{\rm m}^{-3}\,{\rm K}^{-5}$ in all devices.

Table S1. Summary of devices and 3TM parameters.

Device	$\rho_{\rm i}$, nm	L, μm	$\Sigma_{\rm env}$, nW/K
D1	82	1.57	1.21-2.01
D2	82	2.2	0.34
D3	65	2.2	0.9
D4	68	2.2	0.62
D5	76	1.55	0.37
D6	82	1.5	0.61

For device D1 the differential resistance measurements in parallel field (Fig. S1e) show a third Little-Parks lobe indicating good alignment of the NW with the B-field. We chose the misorientation angle $\alpha = 0$ in this device. The two-temperature model (2TM) fit shown by the dotted line in Fig. S1d gives an underestimated value of the electron-phonon cooling power $\Sigma^{\rm 2TM}_{\rm e-ph} = 4\ {\rm nW}\,\mu{\rm m}^{-3}\,{\rm K}^{-5}$.

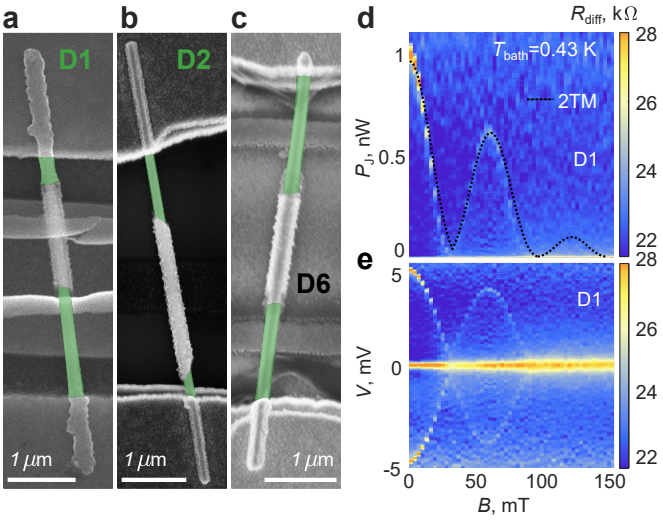


Figure S1. a-c: Scanning electron micrographs of the devices D1, D2 and D6. Regions with an exposed InAs core are false-colored in green. d-e: Color-scale plots of $R_{\rm diff} = dV/dI_{\rm NW}$ vs. parallel field B and Joule power $P_{\rm J}$ (panel c), bias voltage V (panel d) for the device D1. The dotted line is the 2TM fit. The heaters were off throughout the measurement.

COMPENSATION SCHEME FOR CONTACT HEATERS

In the contact heater configuration care was taken to compensate for possible DC (direct current) offsets in the NW circuit in the presence of a finite heater current ($I_{\rm H}$). Typical values of the $I_{\rm H}$ are about three orders of magnitude higher than the NW transport current ($I_{\rm NW}$). In order to disentangle the two currents we employed a compensation circuit shown in Fig. S2 (this particular circuit was used in experiments with D1). Apart from the indicated resistances, the circuit contains two 1 kΩ potentiometers Rtun1 and Rtun2 adjusted to provide virtual grounding of the NW circuit. The tuning procedure is performed in two steps. In the first step, see Fig. S2a, we disconnect the NW wiring and adjust the heater circuit to make sure that the point A is maintained at a virtual ground potential at any $I_{\rm H}$. For this, we adjust $R_{\rm tun1}$ while the heater current is applied untill the voltage measured between the A and the ground is nulled. In the second step, see Fig. S2b, we equalize the potential of the point C to that of A and the virtual ground when the NW wiring is connected. This is achieved by adjusting Rtun2 so that the voltage difference A-C nulls for $I_{\rm NW} = 0$ and for any finite $I_{\rm H}$. This procedure is performed before each experiment with

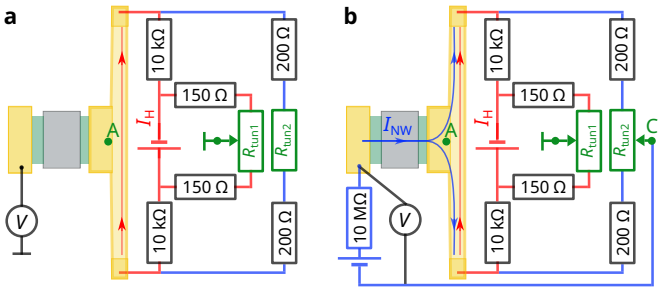


Figure S2. Sketch of the device layout and the complete electrical circuit for the contact heater, along with the tuning procedure for the compensation circuit. The resistor values correspond to those used in experiments with the device D1.

the contact heater. As a result of such compensation the measured P_J is independent of the polarity I_H, see the Figs.1d and 2c in the main text.

JOHNSON NOISE THERMOMETRY

We employ noise thermometry to convert the heater current I_H to the effective temperature rise of the NW, similar to previous experiments [3, 4]. The measurement setup is shown schematically in Fig. S3a. The NW device is connected to a low-temperature resonant tank circuit (inductance $L \approx 3$ μH, total capacitance $C_p \approx 20$ pF dominated by a coaxial cable) with a resonance frequency of about 20 MHz. The tank circuit is placed at the input of a home-made low-noise cryogenic amplifier (LTAmp) with a typical input current noise of $S_I^{\rm Amp} \sim 2 \cdot 10^{-27}$ A^2/Hz. The signal is further amplified by a cascade of room temperature low noise amplifiers (75 dB gain) followed by a bandpass filter and a power detector.

Two load resistors $R_{\rm load} = 39\,\mathrm{k}\Omega$ are connected in parallel to the tank circuit and used for quasi-four-terminal measurements scheme (outputs 1-4 in Fig. S3a). The gain and the input current noise are calibrated with the help of commercial pHEMT transistor (ATF-55143) in parallel to the device. During all other measurements the transistor gate voltage ($V_{\rm tr}$) is zero, which corresponds to pinch-off.

Detector signal

Total input impedance of the circuit is $Z_{\rm total}^{-1}(\omega) = 1/R_{\rm par} + 1/(i\omega L) + i\omega C_p$ where i is the imaginary unit and $R_{\rm par}^{-1} = R_{\rm NW}^{-1} + R_{\rm tr}^{-1} + 2R_{\rm load}^{-1}$ with the NW resistance ($R_{\rm NW}$), transistor resistance ($R_{\rm tr}$). The resistive part generates thermal Johnson–Nyquist noise. This thermal noise through the input impedance producing a voltage

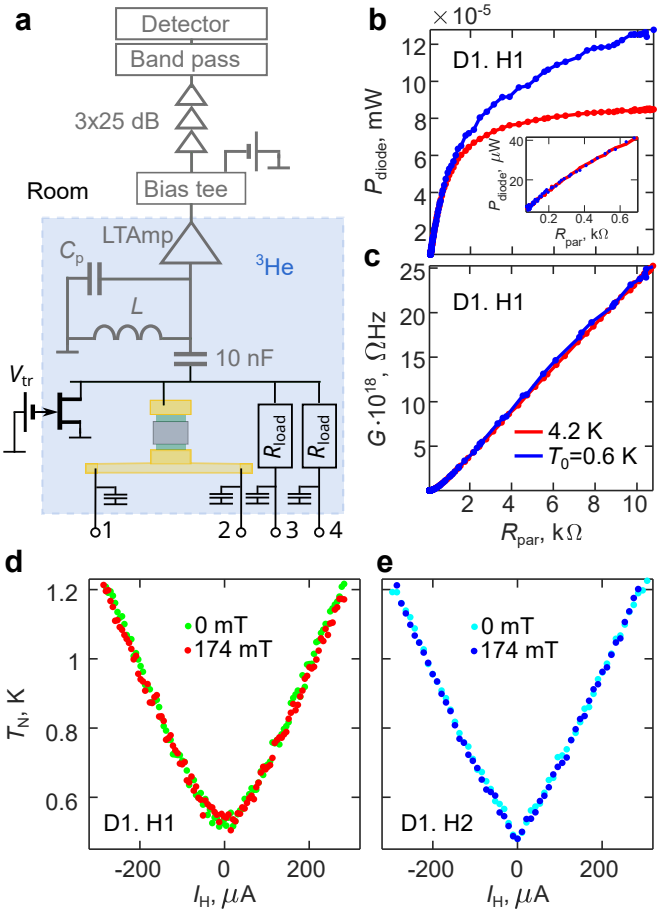


Figure S3. a: Noise measurement scheme. b: Detector power at two temperatures (4.2 K and 0.6 K) for noise calibration for the D1 device (offset subtracted). The higher temperature dataset (red circles) is divided by a factor of $7 = 4.2/0.6$. c: Current noise gain of the circuit at the same two temperatures as a function of the total load resistance $R_{\rm par} = (1/R_{\rm NW} + 1/R_{\rm tr} + 2/R_{\rm load})^{-1}$. d-e: Noise temperature for device D1 in $B = 0$ and $B = 174$ mT.

noise spectral density:

$$S_V^{\rm th}(\omega) = 4k_{\rm B}T \cdot {\rm Re}(Z_{\rm total}(\omega)) = \frac{4k_{\rm B}T_0}{R_{\rm par}} |Z_{\rm total}(\omega)|^2 \tag{S1}$$

The LTAmp adds current noise $S_I^{\rm Amp}$, giving an additional voltage contribution $S_I^{\rm Amp}|Z_{\rm total}(\omega)|^2$. The total voltage noise is then

$$S_V^{\rm total}(\omega) = \left(\frac{4k_BT_0}{R_{\rm par}} + S_I^{\rm Amp}\right)|Z_{\rm total}(\omega)|^2. \tag{S2}$$

The signal passes through a voltage gain G_0 and a bandpass filter $F(\omega)$. The power detector integrates over frequency:

$$P = P_0 + \left(\frac{4k_BT_0}{R_{\rm par}} + S_I^{\rm Amp}\right) G_0^2 \int_0^\infty |F(\omega)|^2 |Z_{\rm total}(\omega)|^2 \frac{d\omega}{2\pi} \tag{S3}$$

P_0 is the constant offset of the detector output signal which is present even in the absence of any input noise. We define the current noise gain of the entire circuit as $G = G_0^2 \int_0^\infty |F(\omega)|^2 |Z_{\rm total}(\omega)|^2 \frac{d\omega}{2\pi}$.

Calibration and shot noise measurement

The calibration relies on two known bath temperatures: 4.2 K and the post-condensation temperature T_0 of the ^{3}He, which is the actual measurement temperature. The detector power (with the offset subtracted) as a function of $R_{\rm par}$ at two temperatures is shown in Fig. S3b for device D1. $R_{\rm par}$ was varied by changing the resistance of the transistor ($R_{\rm tr}$). For the higher temperature (red circles), the data is divided by the temperature ratio $4.2/T_0$. This dataset was acquired during the calibration of heater H1. Based on the assumption that G is independent of the measurement temperature, we slightly adjusted the low bath temperature to a value of $T_0 = 0.6$ K, which is within 5% of the actual thermometer reading. The result is shown in Fig. S3c. Note that the two power dependencies coincide at small $R_{\rm par}$, where the contribution of the amplifier noise is negligible. At the higher $R_{\rm par}$ end, the low temperature data is considerably higher because of the $S_I^{\rm Amp}$ contribution.

When the heater current is turned on, the NW current noise ($S_{\rm I}$) increases. The measurement takes place at $V_{\rm tr} = 0$ V. The measured power modifies according to:

$$P = P_0 + G\left(\frac{8k_BT_0}{R_{\rm load}} + S_{\rm I} + S_{\rm I}^{\rm Amp}\right) \tag{S4}$$

In general, the NW resistance, and thus the current noise gain $G = G(R_{\rm par})$, may depend on the $I_{\rm H}$. In order to take this into account, we define the power offset when the heater is turned off:

$$P^* = P_0 + G^*\left(\frac{4k_BT_0}{R^*_{\rm par}} + S_{\rm I}^{\rm Amp}\right) \tag{S5}$$

where $G^* = G(R^*_{\rm par})$ and $R^*_{\rm par} = R_{\rm par}(I_{\rm H} = 0)$. We extract the NW noise from the power measurement as a function of $I_{\rm H}$:

$$S_{\rm I} = \frac{P - P^*}{G} + \frac{G^*}{G}\frac{4k_BT_0}{R_{\rm NW}(I_{\rm H}=0)} + \left(\frac{G^*}{G} - 1\right)\left(\frac{8k_BT_0}{R_{\rm load}} + S_{\rm I}^{\rm Amp}\right) \tag{S6}$$

In this way we measured the noise power spectral density S_I of the NW and expressed it via the noise temperature $T_N = S_I R_{\rm NW}/(4k_B)$.

In the main text, the heater calibration is performed in the normal state, which is achieved by applying a magnetic field $B = 174$ mT. This field fully suppresses superconductivity in the Al island. We observed no systematic difference in the dependence $T_N(I_{\rm H})$ when S-island was in the superconducting state ($B = 0$), see Figs. S3d-e.

FITTING THE 3TM WITHOUT NOISE THERMOMETRY

For devices in which a direct Johnson noise calibration was unavailable (D2–D6), the effective bath temperature $T^*_{\rm bath}(I_{\rm H})$ was determined via a linear fit based on the known bath and critical temperatures $T_{\rm c}(B)$.

For each device in a fixed magnetic field B, the dependence $P_{\rm J}^{\rm c}(I_{\rm H})$ was measured. Extrapolation of this dependence to zero yielded the critical heater current $I^*_{\rm H}$ at which superconductivity is suppressed even in the absence of transport current, i.e. $P_{\rm J}^{\rm c}(I^*_{\rm H}) = 0$. At this point the effective bath temperature coincides with the superconducting critical temperature: $T^*_{\rm bath}(I^*_{\rm H}) = T_{\rm c}(B)$. At $I_{\rm H} = 0$ the effective bath temperature coincides with the true bath temperature: $T^*_{\rm bath}(I^*_{\rm H} = 0) = T_0$.

We used a linear relationship between $T^*_{\rm bath}$ and the heater current in the interval $0 \le I_{\rm H} \le I^*_{\rm H}$:

$$T^*_{\rm bath}(I_{\rm H}) = T_0 + (T_{\rm c}(B) - T_0)\,\frac{I_{\rm H}}{I^*_{\rm H}}, \tag{S7}$$

which is consistent with the direct calibration by means of noise thermometry in device D1. Using Eq. (S7), we converted $I_{\rm H}$ to $T^*_{\rm bath}$ and fitted the data with the 3TM. The values of $\Sigma_{\rm env}$ obtained for devices D2–D6 in this way are summarized in Fig. 3e of the main text and in Table S1.

COOLING VIA THE INAS CORE

Phonon thermal conductivity of the InAs core

In the main text, we assumed that heat dissipation through the InAs core is negligible. Here we give an upper bound for the heat flux through the core via acoustic phonons in InAs in the ballistic transport regime. We consider a cylindrical InAs NW with cross-sectional area

$S = \pi\rho_{\rm i}^2$. To avoid explicit summation over quantized transverse modes, we adopt an isotropic phonon gas model, which overestimates the actual heat flux.

The heat flux is calculated analogously to the Stefan–Boltzmann law for acoustic phonons. For a single acoustic branch with an index α, the energy flow is written as:

$$\dot{Q}_\alpha = S \int \frac{d^3k}{(2\pi)^3}\, \hbar\omega\, n(\hbar\omega, T)\, v_\alpha \cos\theta, \tag{S8}$$

where k is the phonon wave vector, v_α is the sound velocity, $n(\hbar\omega, T) = (e^{\hbar\omega/k_B T} - 1)^{-1}$ is the Bose–Einstein distribution, and θ is the angle between the phonon wave vector and the NW axis. The integration is performed over the half-space, which takes into account only phonons propagating in one direction along the NW axis. This corresponds to half of the total heat flux from the S-island to the reservoirs via InAs. We neglect possible Kapitza resistance between Al and InAs, which, again, overestimates the heat flux. The volume element in k-space can be expressed as $d^3k = k^2 \cdot 2\pi \sin\theta\, d\theta\, dk$. Converting the radial variable from k to ω via linear spectrum $\omega = v_\alpha k$ yields $d^3k = v_\alpha^{-3}\omega^2 \cdot 2\pi \sin\theta\, d\theta\, d\omega$. After the integration,

$$\dot{Q}_\alpha = \frac{\pi^2 S (k_B T)^4}{120\hbar^3 v_\alpha^2}. \tag{S9}$$

Summing over one longitudinal (velocity v_L) and two transverse (velocity v_T) modes and multiplying by 2 we obtain the total heat flow from the S-island (T_2) to the reservoirs (T_1):

$$\dot{Q}_{ph} = \frac{\pi^2 S k_B^4}{60\hbar^3} \left(\frac{1}{v_L^2} + \frac{2}{v_T^2} \right) \left(T_2^4 - T_1^4 \right). \tag{S10}$$

Using typical InAs values of the sound velocities $v_L = 4300$ m/s, $v_T = 2400$ m/s, and taking $\rho_{\rm i} = 80$ nm, we obtain

$$\dot{Q}_{ph} \approx 40\ \frac{\rm pW}{\rm K^4} \cdot \left(T_2^4 - T_1^4 \right) \tag{S11}$$

This value represents the absolute maximum heat current through the InAs core, which can only decrease if the phonon scattering and Kapitza resistance are taken into account. The critical Joule power measured in experiment is at least an order of magnitude higher, confirming that the dominant cooling pathway is via the surrounding ^{3}He.

Electronic thermal conductivity of the InAs core

For completeness, we estimate the electronic heat flow through the InAs core in the diffusive transport regime. The electronic thermal conductivity obeys the Wiedemann–Franz law: $\kappa_{\rm el}(T) = L_0 \sigma T$, where $L_0 = 2.44 \times 10^{-8}\ \mathrm{W\,\Omega/K^2}$ is the Lorenz number, $\sigma = L_{\rm InAs}/(R_{\rm NW} S)$ is the electrical conductivity, $L_{\rm InAs}$ is the NW length, $R_{\rm NW}$ is the NW resistance, and S is the cross-sectional area.

In the diffusive regime, the heat flow along the NW due to a temperature gradient is given by Fourier's law:

$$\dot{Q}_{\rm el} = -\kappa_{\rm el}(T) S \frac{dT}{dx}, \tag{S12}$$

Separating variables and integrating from the cold end ($x = 0$, $T = T_1$) to the hot end ($x = L_{\rm InAs}$, $T = T_2$) gives

$$\dot{Q}_{\rm el} \int_0^{L_{\rm InAs}} dx = -L_0 \frac{L_{\rm InAs}}{R_{\rm NW}} \int_{T_1}^{T_2} T\, dT, \tag{S13}$$

Cancelling $L_{\rm InAs}$ and taking the absolute value (heat flows from hot to cold),

$$\dot{Q}_{\rm el} = \frac{L_0}{2R_{\rm NW}} \left(T_2^2 - T_1^2 \right). \tag{S14}$$

The final estimate takes into account that $R_{\rm NW}$ is approximately one half of the total NW resistance (~ 10 kΩ) and that the heat flows from the S-island in two directions. Therefore we obtain:

$$\dot{Q}_{\rm el} \sim 5 \frac{\rm pW}{\rm K^2} \cdot \left(T_2^2 - T_1^2 \right). \tag{S15}$$

This is at least two orders of magnitude smaller than the measured critical Joule power, meaning that the contribution of electronic thermal conductance in cooling of the S-island negligible.

COOLING OF THE S-ISLAND VIA ^{3}HE GAS

Here we consider the case of cooling a metallic island in a saturated ^{3}He vapor. The average mean free path of the ^{3}He atom exceeds the size of the S-island and we assume that the atoms are fully thermalized with the metal surface upon collision. The number flux of atoms incident on the unit surface is $\Phi = \frac{n\bar{v}}{4}$, where n is the gas concentration and $\bar{v} = \sqrt{3k_B T_{\rm bath}/m_{\rm He}}$ the root-mean-square speed from the Maxwell–Boltzmann distribution with effective mass $m_{\rm He} = 5 \cdot 10^{-27}$ kg. Using the temperature dependence of the saturated vapor pressure [5], we determine the atom concentration: $n = P_{\rm He}/(k_B T_{\rm bath})$. Each atom transfers an energy

$$\Delta E = \frac{3}{2} k_B (T_{\rm ph} - T_{\rm bath}) \tag{S16}$$

upon equilibration with the S-island at temperature $T_{\rm ph}$. The heat flux per unit area becomes $\frac{Q}{A} = \Phi \Delta E$. Comparing with the 3TM expression $\frac{Q}{A} = G_{\rm env}(T_{\rm ph} - T_{\rm bath})$ gives the environmental thermal conductance

$$G_{\rm env} = \frac{3}{8} P_{\rm He} \sqrt{\frac{3k_B}{m_{\rm He} T_{\rm bath}}}. \tag{S17}$$

COOLING OF THE S-ISLAND VIA LIQUID ^{3}HE

We consider a cylindrical S-island of radius $r_0 = \rho_i + t$ and length $L \gg r_0$, with its surface (phonon) temperature of T_0. The island is embedded in liquid ^{3}He, whose thermal conductivity depends on temperature as $\kappa(T) = \alpha T^m$. Our goal is to find the total heat flux $\dot{Q}$ from the island to the bath at temperature $T_{\rm bath}$ (with $T_0 > T_{\rm bath}$).

We consider a stationary heat conduction equation without internal heat sources in cylindrical coordinates, which defines the heat flux divergence: $\nabla \cdot \mathbf{q} = 0$. The heat flux density q (power per unit area) obeys Fourier's law: $q = -\kappa(T)\, dT/dr$, where r is the radial coordinate. The total heat flux through a surface of area S is $\dot{Q} = Sq$ (the sign of q indicates the direction).

To analyze the heat transfer, we split space around the S-island into two regions. Close to the cylinder (Region I, $r_0 \le r \le R$), the temperature gradient is predominantly radial because $L \gg r_0$; the heat flow is governed by cylindrical symmetry. Far from the cylinder (Region II, $r \ge R$), the heat flow becomes approximately isotropic and spherically symmetric. The matching radius R is taken to be of order L; its optimal value is determined below.

Region I (cylindrical symmetry). For a cylindrical surface of radius r and length L, the total heat flux is $\dot{Q} = -2\pi r L \alpha T^m (dT/dr)$. Separating variables and integrating from the island surface ($r = r_0$, $T = T_0$) to the matching radius ($r = R$, $T = T(R)$) yields:

$$T_0^{m+1} - T(R)^{m+1} = \frac{\dot{Q}(m+1)}{2\pi\alpha L} \ln\left(\frac{R}{r_0}\right). \tag{S18}$$

Region II (spherical symmetry). For a spherical surface of radius r, the total heat flux is $\dot{Q} = -4\pi r^2 \alpha T^m (dT/dr)$. Proceeding similarly, we integrate from $r = R$ ($T = T(R)$) to infinity ($T = T_{\rm bath}$):

$$T(R)^{m+1} - T_{\rm bath}^{m+1} = \frac{\dot{Q}(m+1)}{4\pi\alpha} \frac{1}{R}. \tag{S19}$$

Matching the two regions. Adding equations (6) and (7) eliminates the unknown intermediate temperature at the matching radius $T(R)$:

$$T_0^{m+1} - T_{\rm bath}^{m+1} = \frac{\dot{Q}(m+1)}{2\pi\alpha L} \ln\left(\frac{R}{r_0}\right) + \frac{\dot{Q}(m+1)}{4\pi\alpha} \frac{1}{R}. \tag{S20}$$

Solving for $\dot{Q}$ gives:

$$\dot{Q} = \frac{2\pi\alpha L}{m+1} \left[\ln\left(\frac{R}{r_0}\right) + \frac{L}{2R}\right]^{-1} \left(T_0^{m+1} - T_{\rm bath}^{m+1}\right). \tag{S21}$$

The matching radius R is determined from the condition of maximum cooling power. We find the minimum of the bracket in the denominator with respect to R by differentiation, which yields the optimal value $R = L/2$. Substituting this back gives the final expression:

$$\dot{Q} = \frac{2\pi\alpha L}{m+1} \cdot \frac{1}{\ln\left(\frac{L}{2r_0}\right) + 1} \cdot \left(T_0^{m+1} - T_{\rm bath}^{m+1}\right). \tag{S22}$$

Eq. (S22) provides the effective environmental cooling power $\Sigma_{\rm env}$ used in the three-temperature model (Eq. (1) of the main text). For liquid ^{3}He with thermal conductivity $\kappa(T) = \alpha T^{0.5}$ ($m = 0.5$). We take into account that the liquid occupies only the half-space above the substrate, which reduces the above estimate by two and yields $\Sigma_{\rm env}$ values plotted in Fig. 3e of the main text (dashed line). This model overestimates the experimental value of $\Sigma_{\rm env}$ by approximately a factor of 10. This systematic discrepancy suggests that the heat is not dissipated into a bulk half-space of liquid ^{3}He, but rather into a thin wetting film.

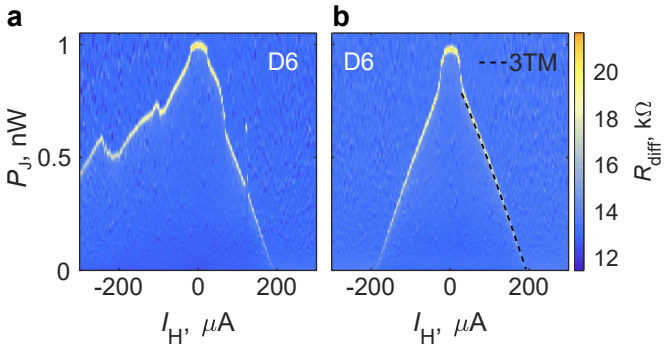


Figure S4. Color-scale plot of the $R_{\rm diff} = dV/dI_{\rm NW}$ as a function of Joule power P_J in the NW and I_H for the device D6. The dashed line represents the fit using the three-temperature model (3TM).

NON-REPRODUCIBLE CRITICAL POWER BEHAVIOR

The dependencies of the critical power on the heater current presented in the main text are obtained in the steady-state regime. The non-steady-state regime refers to a state where the critical Joule power P_J^c varies randomly and irreproducibly with time. After cooling the device chamber from 4.2 K down to the operating temperatures, approximately one hour is required to reach the steady-state regime. We attribute this behavior to the peculiarities of ^{3}He cooling and the possible formation of bubbles and boiling of ^{3}He near heaters. Figure S4 illustrates the approach to the steady-state regime for device D6, which exhibits a tiny hysteresis of the I-V curves near the superconducting-normal transition in the S-island. Two consecutive maps of the

differential resistance versus Joule power and heater current I_H are shown in Fig. S4a and Fig. S4b. In Fig. S4a, the dependence P_J^c on the $|I_H|$ is asymmetric, non-monotonic and irreproducible. This is a non-steady-state regime, which we attribute to random variations of the Σ_{env}. Note that the heater current is swept from negative to positive values and the behavior at $I_H > 0$ is more regular. By contrast, in Fig. S4b the behavior is stable, allowing a fit based on the three-temperature model (3TM), which is shown by the dashed line. This fit is used in Fig. 3e of the main text.

In the regime of small heater currents, a distinct reproducible feature is observed in Fig. S4b. Here, the critical Joule power shows a local flat maximum that is not captured by the 3TM with the constant Σ_{env}. This feature is common to all devices and is reproducibly observed at low enough bath temperatures, as also visible in Fig. 1d of the main text. The feature disappears above approximately T_{bath} ≈0.4 K, that is why it is absent in Figs. 2c and 3a of the main text. We attribute this behavior to a change (decrease) of the environmental cooling parameter Σ_{env} at increasing the heater current. Although the microscopic details of this phenomenon are not understood, a plausible explanation is that the thickness of the ^{3}He layer wetting the NW decreases at increasing I_H.

1. E. V. Shpagina, E. S. Tikhonov, D. Ruhstorfer, G. Koblmüller, and V. S. Khrapai, «Fate of the Superconducting State in Floating Islands of Hybrid Nanowire Devices», Physical Review B **109**, L140501 (2024).
2. E. V. Shpagina, E. S. Tikhonov, D. Ruhstorfer, G. Koblmüller, and V. S. Khrapai, «Superconducting bistability in floating Al islands of hybrid Al/InAs nanowires», Phys. Rev. B **112**, L140503 (2025).
3. E S Tikhonov, D V Shovkun, D Ercolani, F Rossella, M Rocci, L Sorba, S Roddaro, and V S Khrapai, «Local Noise in a Diffusive Conductor», Scientific Reports **6**, 30621 (2016).
4. E. S. Tikhonov, «Noise Thermometry Applied to Thermoelectric Measurements in InAs Nanowires», Semicond. Sci. Technol. **31**, 104001 (2016).
5. S. G. Sydoriak and T. R. Roberts, «Thermodynamic Properties of Liquid Helium Three. Vapor Pressures below 1°K», Physical Review **106**, 175 (1957).